Spectroscopy and dynamics of $Er^{3+}:Y_2SiO_5$ at 1.5 μm

Thomas Böttger*
Department of Physics, University of San Francisco, 2130 Fulton Street, San Francisco, California 94117, USA
and Department of Physics, Montana State University, Bozeman, Montana 59717, USA

Y. Sun†
Department of Physics, Montana State University, Bozeman, Montana 59717, USA
and Department of Physics, The University of South Dakota, Vermillion, South Dakota 57069, USA

C. W. Thiel‡ and R. L. Cone§
Department of Physics, Montana State University, Bozeman, Montana 59717, USA
(Received 8 April 2006; published 21 August 2006)

We present the results of detailed site-selective spectroscopy performed on the $^4I_{15/2} \leftrightarrow {}^4I_{13/2}$ transition of $Er^{3+}:Y_2SiO_5$ at 1.5 μm. New determinations of the $^4I_{13/2}$ and $^4I_{15/2}$ crystal-field-level structure for the two crystallographically inequivalent Er^{3+} sites have been made. The fluorescence dynamics of the metastable $^4I_{13/2}:Y_1$ excited state was investigated, showing exponential decays for Er^{3+} at both crystallographic sites with fluorescence lifetimes of 11.4 ms for site 1 and 9.2 ms for site 2. Exceptionally sharp inhomogeneous absorption lines of 180, 390, and 510 MHz were observed in 0.0015% $Er^{3+}:Y_2SiO_5$, 0.005% $Er^{3+}:Y_2SiO_5$, and 0.02% $Er^{3+}:Y_2SiO_5$ crystals, respectively. The g-values for the lowest energy $^4I_{15/2}$ (Z_1) and $^4I_{13/2}$ (Y_1) doublets were measured to be 5.5 and 4.6 for site 1 and 15.0 and 12.9 for site 2 when the magnetic field was oriented along the crystal's $\boldsymbol{D}_1$ axis.

DOI: 10.1103/PhysRevB.74.075107 PACS number(s): 71.70.Ch, 78.40.−q, 42.62.Fi, 71.70.Ej

I. INTRODUCTION

The optical material $Er^{3+}:Y_2SiO_5$ has recently received considerable attention for spatial spectral holography (SSH) and spectral hole burning (SHB) applications because of its narrow homogeneous linewidths and long coherence lifetimes. It exhibits the narrowest homogeneous optical resonance yet reported in a solid with a linewidth of $\Gamma_h = 73$ Hz.[1,2] In addition, optical transitions located in the important 1.5 μm optical communication band make it appealing for technological applications, and conversely, the well-developed infrastructure for 1.5 μm telecommunication devices can be exploited for spectroscopy and demonstrations of SSH and/or SHB devices. This material also has been investigated for solid-state laser applications[3] because of good chemical and thermomechanical properties as well as the potential for high rare-earth doping.

In 1997, Macfarlane *et al.*[4] measured the first two-pulse photon echoes in $Er^{3+}:Y_2SiO_5$ and observed dephasing times up to 580 μs, triggering a number of important SSH and/or SHB proof-of-principle device demonstrations. These demonstrations were motivated by the desire to develop SHB technologies that would enable all-optical memory, switching, and processing at communication wavelengths.[5,6] In addition, because of its narrow homogeneous linewidth, $Er^{3+}:Y_2SiO_5$ has been used as an excellent frequency reference, providing sub-kHz laser frequency stability,[7–9] which proved important both for frequency resolution and signal averaging by "accumulated gratings" in SSH and/or SHB applications; it is important also to note that the lifetime of the frequency reference is exactly the material storage time and that vibrational sensitivity is greatly reduced by using the same crystal as processor and reference. This technique, combined with material optimization,[1] has significantly extended processing bandwidths as demonstrated at cryocooler temperatures of 4.2 K.[10] More recently, $Er^{3+}:Y_2SiO_5$ has also been exploited in high-resolution radio-frequency spectral analysis[11] and amplification of photon echoes.[12]

In spite of the excellent material properties that make $Er^{3+}:Y_2SiO_5$ attractive for these applications, many spectroscopic properties critical for these applications have not yet been reported. The work reported here was motivated by the need for detailed knowledge of the excited-state lifetimes, crystal-field-level structure, and ground- and excited-state g-values that are crucial for achieving long dephasing times. The excited-state lifetimes establish an upper limit for the material storage time, and the crystal-field-level structure is important for pumping pathways; these material properties are important for both lasers and SSH applications.

The optical absorption lines of Er^{3+} arise from transitions between different energy levels of the odd numbered $4f^{11}$ electron configuration.[13–16] In addition to the forced electric dipole transitions typical for higher energy visible rare-earth transitions, the infrared $^4I_{15/2} \rightarrow {}^4I_{13/2}$ absorption transitions can be magnetic dipole in character, following the selection rules $\Delta S = \Delta L = 0$, $\Delta J = 0, \pm 1$. For the levels of interest, the angular momentum J is nominally a good quantum number, and the $2J+1$-fold degenerate energy levels give rise to multiplets labeled by J. The reduced crystal-field symmetry causes partial lifting of the $2J+1$-fold degeneracy, and as a consequence of the odd number of electrons, Kramers theorem[17] dictates that each J multiplet can be split into a maximum of $J+\frac{1}{2}$ doubly degenerate crystal-field levels. Consequently, the $^4I_{15/2}$ ground multiplet can be split into eight Kramers doublets and the $^4I_{13/2}$ multiplet into seven. Application of a magnetic field lifts the remaining degeneracy, and each crystal-field level splits into two Zeeman

sublevels. For arbitrary directions of the applied magnetic field there are two magnetically inequivalent sites for each crystallographic site, resulting in complex Zeeman spectra.

Previous absorption and emission studies on $Er^{3+}:Y_2SiO_5$ by Li *et al.*[3] were carried out in the context of solid-state laser material development using highly doped (up to 10 at.% Er^{3+} concentration) powder and single-crystal samples for temperatures between $T=10$ and 300 K. Those measurements yielded the expected 16 crystal-field components of the $^4I_{15/2}$ ground state for the two crystallographical sites and 14 components of the $^4I_{13/2}$ excited state; however, the assignments of transitions to the two crystallographic sites reported by Li *et al.* were uncertain because assignments were made without the use of site-selective spectroscopy.

Expanding on this previous work, broadband absorption experiments and site-selective fluorescence experiments were used to resolve the identification and site assignments. Absorption measurements located the excited-state crystal-field levels, and site-selective fluorescence and fluorescence excitation allowed us to confidently assign the $^4I_{13/2}$ excited and $^4I_{15/2}$ ground-state-level structure to the Er^{3+} crystallographic sites. Time-resolved fluorescence spectroscopy was used to measure the excited-state lifetime, which is important for lasers and also determines the storage time and maximum achievable coherence time in SSH applications.

The practical operation of $Er^{3+}:Y_2SiO_5$ in SSH and/or SHB devices generally requires the application of an external magnetic field to achieve long coherence times through the suppression of spectral diffusion. A Zeeman-level splitting large compared to the thermal energy k_BT reduces thermal populations in the upper Zeeman level and suppresses spectral diffusion induced by Er^{3+} spin flips.[1,8,18,19] Ground and excited state g-values were precisely determined by high-resolution laser absorption experiments.

Laser absorption spectroscopy was also used to study the Er^{3+} dopant concentration dependence on the width of the inhomogeneous absorption line. Exceptionally sharp inhomogeneous lines were observed over the concentration range $0.0015\%\,Er^{3+}$–$0.02\%\,Er^{3+}$.

II. MATERIAL

The $Er^{3+}:Y_2SiO_5$ crystals were grown by Scientific Materials, Inc. of Bozeman, Montana using the Czochralski method. The $Er^{3+}:Y_2SiO_5$ crystals investigated had nominal Er^{3+} -dopant concentrations of 2% (growth No. 0-84), 0.02% (growth No. 2-430), 0.005% (growth No. 6-429), and 0.0015% (growth No. 1-544) atomic percent substitution for Y^{3+}. For broadband absorption, the Er^{3+} concentration was 2%, whereas for fluorescence experiments 0.0015% Er^{3+} concentration was chosen to minimize radiation trapping and excitation transfer or migration among sites. For Zeeman laser absorption experiments, we used 0.0015% dopant concentration to take advantage of the resolution afforded by the very sharp 180 MHz full width at half maximum (FWHM) inhomogeneous linewidths. Laser absorption experiments on the 0.0015%, 0.005%, and 0.02% crystals were also used to investigate the inhomogeneous linewidth dependence on Er^{3+} concentration. To get accurate measurements on the inhomogeneous linewidths, laser absorption experiments could only be carried out using these low concentration samples to avoid overabsorption and the associated line shape distortion.

The crystal Y_2SiO_5 belongs to the space group C_{2h}^6 ($C2/c$, No. 15) with eight formula units per monoclinic cell. The Y^{3+} ions occupy two crystallographically inequivalent sites of C_1 symmetry[20] and the Er^{3+} ions substitute for Y^{3+} host ions without charge compensation. The Er^{3+} ionic radius is very similar to that of Y^{3+}, and the occupancy of the two Y^{3+} sites by Er^{3+} dopant ions is believed to be nominally equal, unlike the cases of $Pr^{3+}:Y_2SiO_5$ and $Eu^{3+}:Y_2SiO_5$, which we studied earlier.[21] All crystals were transparent and appeared colorless.

The material $Er^{3+}:Y_2SiO_5$ has three mutually perpendicular optical-extinction axes, the crystal's **b** axis equivalent to the $\langle 010\rangle$ direction, and the $\mathbf{D}_1$ and $\mathbf{D}_2$ axes correspond to optical-extinction directions when the sample is viewed along the **b** axis between crossed polarizers.[3] All crystals were oriented, cut, and optically polished perpendicular to the three optical-extinction axes. The orientation of the optical-extinction directions $\mathbf{D}_1$ and $\mathbf{D}_2$ with respect to the crystal cuts was verified by viewing the crystals between crossed polarizers.

For SSH applications and fundamental studies of line-broadening mechanisms and spectral diffusion, extremely long coherence times can be achieved because the constituent elements of the host material Y_2SiO_5 have small magnetic moments ($-0.137\mu_N$ for ^{89}Y) or a small natural abundance of magnetic isotopes (4.7% with $-0.554\mu_N$ for ^{29}Si, 0.04% with $-1.899\mu_N$ for ^{17}O).[4] By minimizing the magnetic moments in the host lattice, dephasing due to nuclear and electronic spin fluctuations has been dramatically reduced.

III. EXPERIMENTAL

For absorption, a 2% $Er^{3+}:Y_2SiO_5$ crystal was immersed in a liquid-helium bath held at $T=1.95$ K using an Oxford Instruments SpectroMag cryostat with four windows providing optical access. Operating at $T=1.95$ K ensured that only the lowest crystal-field level Z_1 of the $^4I_{15/2}$ J multiplet was initially populated. The light **k** vector was aligned parallel to the **b** axis along a 2 mm path, and the other crystal dimensions were 3 mm parallel to $\mathbf{D}_1$ and 4 mm parallel to $\mathbf{D}_2$. For absorption measurements, a tungsten filament was imaged inside the crystal and a color filter with bandpass between 950 and 2900 nm was used to eliminate visible light that could be transmitted at second order by the spectrometer. A Glan-Thompson polarizer selected the light polarization before the sample. Transmitted light through the crystal was spectrally resolved by a SPEX 1000M spectrometer with a 600 line/mm grating blazed at 1.5 μm, giving 1.6 nm/mm dispersion at the exit slit. Entrance and exit slit widths were 20 μm, giving a bandpass of 0.03 nm or 0.13 cm^{-1} over the wavelength ranges studied here. The transmitted light signal was measured by a liquid nitrogen-cooled Applied Detector Corporation Model C3L Germanium detector and then amplified, digitized, and recorded with signal averaging that

typically involved 1000 readings at each wavelength step.

Weak interference fringes caused by the Germanium detector window and crystal faces as well as the rich absorption spectrum of atmospheric water vapor were observed in the recorded absorption spectra. The water lines provided a convenient calibration for the spectrum using the HITRAN database.[22] The interference fringe background was minimized using a wedge-shaped yttrium aluminum garnet (YAG) window in place of the original detector window, and the transmission data were corrected for the remaining weak interference fringes using a software-fitting routine.[23] Final calibrations of the spectra were verified using a narrowband external cavity diode laser (ECDL) as a marker in the spectrum with the laser wavelength determined to very high precision (~100 MHz) with a Burleigh WA-1500 wavemeter that was calibrated in our laboratory to a NIST traceable hydrogen cyanide absorption cell.[24]

For site-selective fluorescence experiments, the narrowband ECDL was used to individually excite each absorption line. For these experiments, a 0.0015% $Er^{3+}:Y_2SiO_5$ crystal was aligned with the laser **k** vector parallel to the $\mathbf{D}_1$ axis along a 5 mm path, and other crystal dimensions were 3 mm along **b** and 4 mm along $\mathbf{D}_2$. The fluorescence was collected at an angle of 90° with respect to the laser beam and focused onto the spectrometer entrance slit. The spectrally filtered fluorescence was detected by a liquid-nitrogen-cooled Hamamatsu Photocool series PC176TSCE005 near-infrared photomultiplier tube (PMT). The fluorescence excitation wavelengths for the ECDL were monitored with the Burleigh WA-1500 wavemeter, ensuring site-selective pumping. Laser absorption of the individual $^4I_{13/2}$ levels was also verified by scanning the ECDL over the respective absorption line and detecting the transmitted intensity with an InGaAs PIN photodiode.

To determine the fluorescence lifetime of the metastable $^4I_{13/2}$ state, a laser pulse was used to pump the $^4I_{15/2}:Z_1$ to $^4I_{13/2}:Y_2$ absorption for a single site. The output of the ECDL was amplified with an erbium-doped fiber amplifier, and a 165 MHz acousto-optic modulator with a transition time $\ll 1$ μs gated the amplified laser beam to produce sharp-edged 1 ms pulses at a 10 Hz repetition rate with a peak optical power of 1.8 mW at the sample. The $^4I_{15/2}:Z_1 \rightarrow {}^4I_{13/2}:Y_2$ transition was pumped to allow the laser and fluorescence signals to be spectrally separated. Rapid nonradiative relaxation from Y_2 to Y_1 within the $^4I_{13/2}$ J multiplet of that site resulted in fluorescence occurring from $^4I_{13/2}:Y_1$ to $^4I_{15/2}:Z_1-Z_8$. Fluorescence intensity was recorded as a function of time with the Hamamatsu PMT, with the SPEX spectrometer tuned to individual $^4I_{13/2}$ to $^4I_{15/2}$ transitions. The low 0.0015% Er^{3+} concentration minimized radiative energy trapping effects that can artificially lengthen fluorescence decay times. The Burleigh WA-1500 wavemeter continuously monitored the laser wavelength, and the transmitted intensity through the crystal was monitored with an InGaAs photodetector to verify resonance with the absorption lines for pulsed excitation.

To measure the Zeeman-level splitting, a 0.0015% $Er^{3+}:Y_2SiO_5$ crystal was used. Very sharp 180 MHz FWHM inhomogeneous lines in this crystal and the narrowband single-mode continuously tunable ECDL enabled laser absorption experiments with an accuracy approaching electron paramagnetic resonance techniques. The crystal was placed inside the Oxford Instruments Spectromag cryostat with the magnetic field along $\mathbf{D}_1$ and the laser **k** vector along **b**. The laser was polarized with the electric field vector **E** along $\mathbf{D}_2$. To minimize spectral hole burning, the laser light was attenuated with neutral density filters and propagated through the crystal without focusing. To observe all possible transitions between the Zeeman-split ground- and excited-states and to further minimize spectral hole burning, a temperature of $T=5$ K was chosen. Transmitted light through the crystal was detected with the InGaAs PIN photodiode and displayed on the oscilloscope. The laser absorption spectra were recorded by scanning the ECDL over the spectral region of interest. To calibrate the spectra, the heterodyne signal between the scanning ECDL and a second fixed-frequency reference ECDL was detected on a separate InGaAs PIN photodiode, and displayed simultaneously with the laser-absorption scan. The narrow spike of the beat signal, whose width was established by the 125 MHz bandwidth of the InGaAs PIN photodiode, provided an accurate frequency marker that was manually tuned to each absorption line-center by tuning the second ECDL. Marker frequencies, and therefore line center frequencies could be measured with a Burleigh wavemeter to an absolute accuracy of ±100 MHz.

The dependence of the inhomogeneous linewidth on Er^{3+}-dopant concentration and the dependence of the absorption strength on the laser's polarization was investigated in 0.0015%, 0.005%, and 0.02% $Er^{3+}:Y_2SiO_5$ with polarized laser-absorption measurements in zero magnetic field using the same experimental conditions and crystal orientation as described for the Zeeman laser-absorption experiments. The polarization of the laser before the sample was selected with a half-wave plate and Glan-Thompson polarizer. Sample

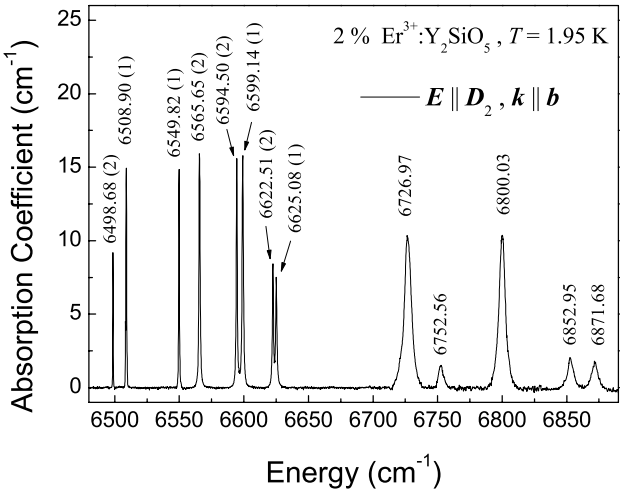

FIG. 1. Absorption spectrum polarized $\mathbf{E}\|\mathbf{D}_2$ for 2% $Er^{3+}:Y_2SiO_5$ at $T=1.95$ K. Water-absorption lines and interference fringes have been removed for better visibility. Absorption-line center energies are given in wave numbers (cm^{-1}), and the numbers in parentheses show the crystallographic site assignments from site-selective fluorescence experiments. Laser site-selective excitation was not available above 6700 cm^{-1}, so several $^4I_{13/2}$ levels were not assigned to specific sites.

thicknesses were chosen accordingly to avoid distortion of the linewidths by overabsorption. The crystal dimensions were 2 mm along **b**, 12 mm along $\mathbf{D}_1$, and 15 mm along $\mathbf{D}_2$ for the 0.0015% sample; 1.27 mm along **b**, 4 mm along $\mathbf{D}_1$, and 5 mm along $\mathbf{D}_2$ for the 0.005% sample; and 0.5 mm along **b**, 5.2 mm along $\mathbf{D}_1$, and 4 mm along $\mathbf{D}_2$ for the 0.02% sample. Small nonlinearities in the laser-absorption line-shape scans were removed with a software routine[23] by simultaneously recording the laser transmission spectrum through a high-finesse Fabry-Pérot interferometer and using its calibrated frequency comb as a reference.

IV. RESULTS AND DISCUSSION

Absorption measurements mapped the crystal-field levels of the $^4I_{13/2}$ J multiplet. Two interspersed sets of absorption lines from both Er^{3+} sites were observed with each site experiencing slightly different crystal-field splittings in the Y_2SiO_5 host. The 2% Er^{3+} concentration proved ideal to obtain large absorption signals, while also avoiding overabsorption. Figure 1 shows a typical polarized $\mathbf{E}\|\mathbf{D}_2$ absorption spectrum at $T=1.95$ K for the 2% $Er^{3+}:Y_2SiO_5$ crystal. Waterline absorption and interference fringes have been removed from the spectrum for clarity. The spectrum contains very sharp well-separated absorption lines; 13 out of the possible 14 lines for the $^4I_{13/2}$ J multiplet for the two sites were observed. The missing line might be very weak or hidden under the envelope of another strong line. Detected linewidths progressively increase with energy within a J multiplet because of lifetime broadening arising from spontaneous phonon emission from the upper to the lower levels of the $^4I_{13/2}$ J multiplet. Line centers were precisely determined by fitting each absorption line. Energies in wave numbers are indicated above each line, and corresponding site assignments are given in parentheses.

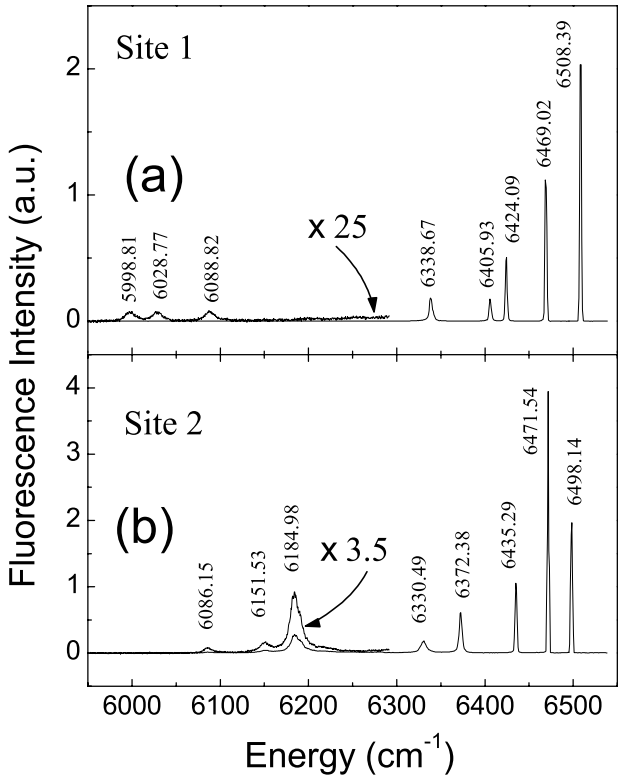

FIG. 2. Site-selective fluorescence spectra for 0.0015% $Er^{3+}:Y_2SiO_5$ at $T=10$ K; line-center energies are given in wave numbers (cm^{-1}). (a) Laser excitation of site 1 $^4I_{15/2}(Z_1) \rightarrow {}^4I_{13/2}(Y_2)$. (b) Laser excitation of site 2 $^4I_{15/2}(Z_1) \rightarrow {}^4I_{13/2}(Y_2)$.

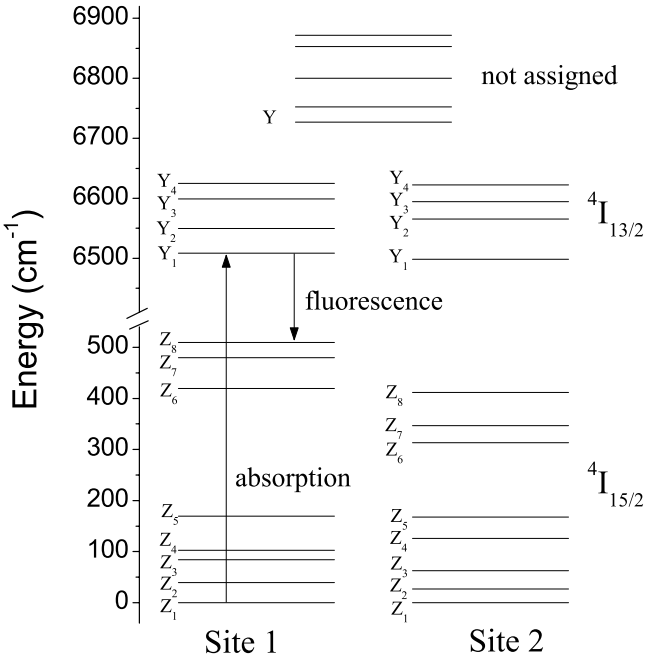

FIG. 3. Crystal-field energy levels of $^4I_{15/2}$ and $^4I_{13/2}$ multiplets in wave numbers for $Er^{3+}:Y_2SiO_5$ determined from absorption and site-selective fluorescence excitation for site 1 and site 2.

To unambiguously assign the observed $^4I_{13/2}$ levels to a specific crystallographic site and also to selectively assign the energy levels of the $^4I_{15/2}$ J multiplet, site-selective fluorescence experiments were performed. When individually pumping the absorption lines, only one of the two distinct fluorescence spectra was observed, and that allowed each crystal-field level of the $^4I_{15/2}$ ground state and $^4I_{13/2}$ to be assigned to site 1 or site 2. Due to the limited tuning range of the available ECDL, it was not possible to pump levels above the $^4I_{13/2}:Y_4$ level, so levels above 6700 cm^{-1} could not be assigned to a specific site using this method.

Figure 2(a) shows a typical fluorescence spectrum excited from the $^4I_{13/2}:Y_1$ level of site 1 at a temperature of $T=10$ K, and Fig. 2(b) shows the unique spectrum for site 2. All of the eight possible lines for each site were clearly identified. Fluorescence line centers were obtained from a fitting routine and are labeled in the graph.

The crystal-field level structure of $Er^{3+}:Y_2SiO_5$ determined from absorption and site-selective fluorescence experiments is shown in Fig. 3. The ground-state $^4I_{15/2}$ crystal-field levels have been labeled Z_1-Z_8 and the $^4I_{13/2}$ excited-state crystal-field levels have been labeled Y_1-Y_4; higher lying Y_n assignments have not been determined, but for our purposes in SSH applications, knowledge of the Y_1-Y_4 assignments is more than sufficient. Table I summarizes the crystal-field level structure of the $Er^{3+}:Y_2SiO_5$ $^4I_{15/2}$ and $^4I_{13/2}$ manifolds obtained in this work.

TABLE I. Crystal-field level energies for $Er^{3+}:Y_2SiO_5$ as determined from absorption and site-selective fluorescence experiments.

	Label	Site 1	Site 2	Unassigned[a]
$^4I_{13/2}$ energies (cm^{-1})				6871.68
				6852.95
				6800.03
				6752.56
				6726.97
	Y_4	6625.08	6622.51	
	Y_3	6599.14	6594.50	
	Y_2	6549.82	6565.65	
	Y_1	6508.39	6498.14	
$^4I_{15/2}$ energies (cm^{-1})	Z_8	509.58	411.99	
	Z_7	479.62	346.61	
	Z_6	419.57	313.16	
	Z_5	169.72	167.65	
	Z_4	102.46	125.76	
	Z_3	84.3	62.85	
	Z_2	39.37	26.6	
	Z_1	0	0	

[a]Limited tuning range of diode laser prevented pumping of these levels.

The excited-state lifetime T_1 establishes an upper bound for the achievable coherence lifetime T_2 through the relation $T_2 \leqslant 2T_1$.[25,26] In addition, T_1 establishes the spectral hole lifetime for population storage in the excited state, and it is important for energy storage in lasers. Figure 4(a) shows the measured $^4I_{13/2}:Y_1 \rightarrow {}^4I_{15/2}:Z_1$ fluorescence decay for site 1 and Fig. 4(b) shows the decay for site 2, both at a temperature of $T=10$ K. The observed fluorescence decays were exponential over several decades, and exponential least-squares fits to the data are shown as solid lines. A fluorescence lifetime of $T_1=11.44\pm0.01$ ms was obtained for site 1 from the exponential fit, whereas $T_1=9.20\pm0.01$ ms was obtained for site 2. The ultralow Er^{3+} concentration of 0.0015% used in our experiments minimized the effect of radiation trapping on the observed fluorescence lifetimes. During a radiative energy-trapping process, the emitted photon is reabsorbed (trapped) and then reemitted, slowing down the overall observed fluorescence. The nearly negligible effect of radiation trapping in our experiments was confirmed by the minimal effect of temperature (a decrease of 0.5 ms in lifetime was observed by increasing the sample temperature to $T=40$ K) and excitation energy on the observed lifetimes. Also, observed lifetimes were unaffected by varying the spatial location of excitation (edge vs center of the crystal). In contrast, pronounced variations in the fluorescence lifetimes with temperature and excitation location were observed by Li *et al.*[3] for $Er^{3+}:Y_2SiO_5$ single crystals of significantly higher dopant concentrations of 1% and 10%. Li *et al.* attributed these variations to radiative energy trapping making it very difficult to give a definite value for the infrared fluorescence radiative lifetime.

From this perspective, our measured T_1 values of 11.4 ms for site 1 and 9.2 ms for site 2 establish an upper limit for the fluorescence lifetime of the $^4I_{15/2}:Y_1$ level in $Er^{3+}:Y_2SiO_5$ materials. Further independent evidence for the accuracy of our measurements, however, is provided by stimulated-photon-echo experiments[18] that established a limit for the fluorescence lifetime of site 1 of $T_1 \geqslant 9.8$ ms, closely approaching the $T_1=11.4$ ms value reported in this paper.

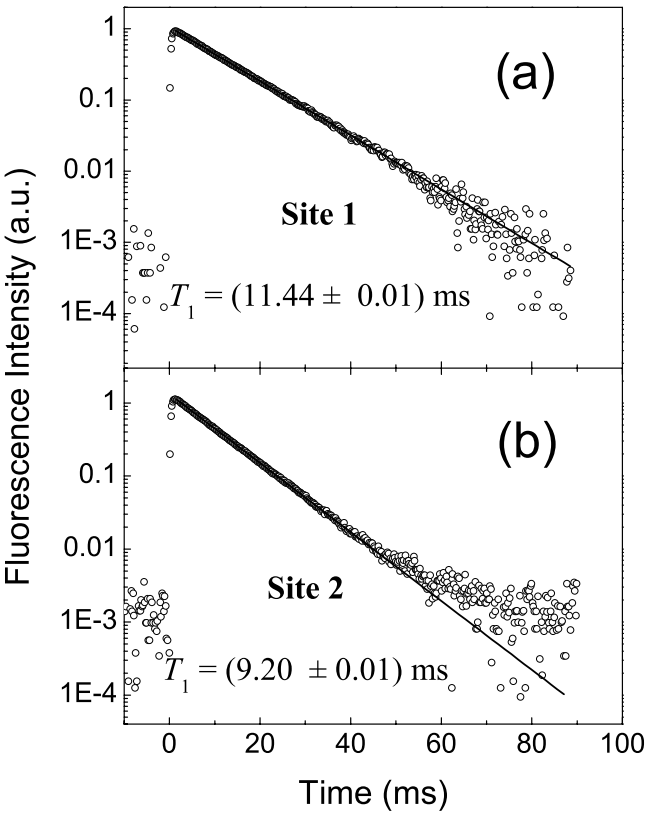

FIG. 4. Fluorescence decay for 0.0015% $Er^{3+}:Y_2SiO_5$ $^4I_{13/2}(Y_1) \rightarrow {}^4I_{15/2}(Z_1)$ transition at $T=10$ K; (a) site 1, (b) site 2. Straight lines correspond to exponential least-square fits to the data. The rise time is indicative of the excitation pulse duration.

Laser-absorption spectroscopy was used to investigate the dependence of the exceptionally narrow inhomogeneous linewidth of the site 1 $^4I_{15/2} \leftrightarrow {}^4I_{13/2}$ transition at 6508.39 cm^{-1} on Er^{3+}-dopant concentration. The peak optical-absorption coefficient, which is important for determining signal-detection levels required in a given SHB and/or SSH application, also depends strongly on the Er^{3+}-dopant concentration due to changes in both line strength and linewidth. Typical results are shown in Fig. 5 for 0.0015%, 0.005%, and 0.02% $Er^{3+}:Y_2SiO_5$ for $\boldsymbol{E}\|\boldsymbol{D}_2$. The relative Er^{3+} concentration of each crystal was confirmed by comparing the integrated absorption coefficients. The strongest absorption for site 1 was found for $\boldsymbol{E}\|\boldsymbol{D}_2$. A 50% weaker absorption was observed for $\boldsymbol{E}\|\boldsymbol{D}_1$ for all crystals as shown in Fig. 6 for 0.005% $Er^{3+}:Y_2SiO_5$ at $T=5$ K. The inhomogeneous line profiles in all crystals were accurately described by Lorentzian lineshapes with FWHM of 180 MHz for 0.0015% $Er^{3+}:Y_2SiO_5$, 390 MHz for 0.005% $Er^{3+}:Y_2SiO_5$, and 510 MHz for 0.02% $Er^{3+}:Y_2SiO_5$. Inhomogeneous widths are generally caused by departures from crystalline perfection and by strain due to ionic-radius mis-

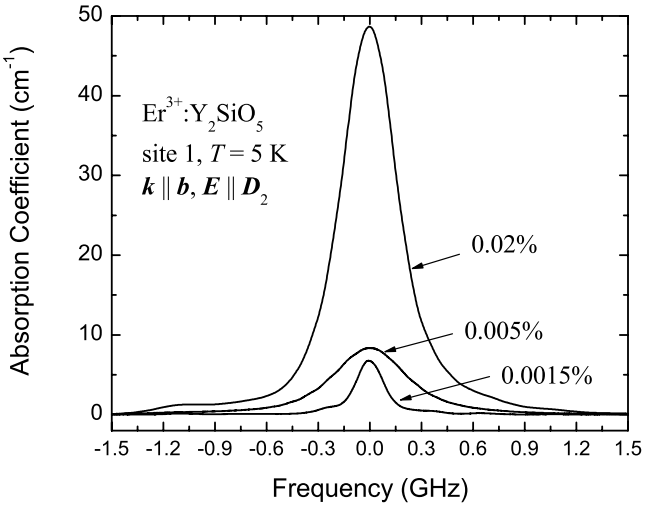

FIG. 5. Laser-absorption spectra polarized $\mathbf{E}\|\mathbf{D}_2$ and $\mathbf{k}\|\mathbf{b}$ for 0.0015%, 0.005%, and 0.02% Er^{3+}:Y_2SiO_5 at T=5 K.

match between the dopant ion and Y^{3+} ions or by impurities. Narrow inhomogeneous widths are expected for the Er^{3+}:Y_2SiO_5 crystal, as the ionic-radius mismatch between Er^{3+} ions and Y^{3+} ions is very small causing only a small strain contribution to the inhomogeneous linewidth. The effective ionic radii for a coordination number of eight for Er^{3+} is 1.004 Å, whereas for Y^{3+} it is 1.019 Å.[27] While our inhomogeneous linewidth numbers appear to indicate a significant increase in inhomogeneous linewidth with Er^{3+} concentration, we should caution that results from other measurements[28] suggest that variations in linewidth for these ultralow doping levels are only weakly dependent on Er^{3+} concentration. Furthermore, contributions to the inhomogeneous linewidth by weak disorder in the Y_2SiO_5 crystal can also lead to significant variations in inhomogeneous linewidths between nominally identical samples.[29]

These narrow inhomogeneous linewidths are attractive for laser-frequency stabilization applications as they can be directly used as frequency references.[30] Furthermore, in the presence of SHB at liquid helium temperatures, the narrow inhomogeneous line can be incorporated in a hybrid locking technique where a continuously regenerated spectral hole in the inhomogeneously broadened optical absorption is used as the short-term frequency reference, while a variation on the locking technique allows simultaneous use of the inhomogeneously broadened absorption line as a long-term reference.[7] This hybrid locking technique dramatically improves long-term laser frequency stability without impacting the stability over short times derived from the spectral hole.

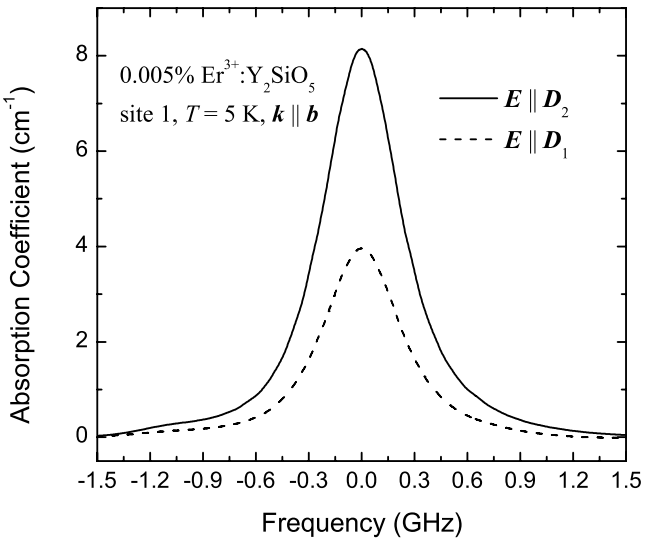

FIG. 6. Polarized laser-absorption spectra $\mathbf{k}\|\mathbf{b}$ for 0.005% Er^{3+}:Y_2SiO_5 at T=5 K.

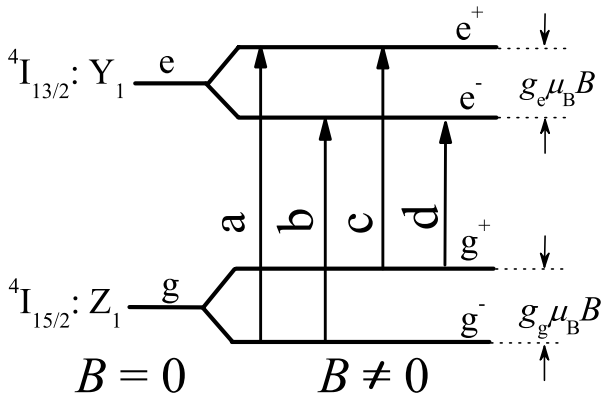

FIG. 7. Transition labeling scheme for the $^4I_{15/2}(Z_1) \rightarrow {}^4I_{13/2}(Y_1)$ transition in a magnetic field.

It should be mentioned that with current material development[31] the inhomogeneous linewidths of Er^{3+}:Y_2SiO_5 can be tailored to give substantially broader widths when bandwidths greater than 20 GHz are needed for SHB and/or SSH applications in high-speed optical processing.

In SHB and/or SSH applications, the homogeneous linewidth of the Er^{3+} ions can evolve over the excited-state lifetime T_1 by Er^{3+}-Er^{3+} magnetic dipole interactions. The scale of these interactions is set in part by the magnetic moments of the Er^{3+} ions. To freeze out the population of the upper Zeeman component of the ground state, and thus suppress spectral diffusion due to Er^{3+} spin flips, we wish to have large g-values. Examination of models for the spectral diffusion process shows that one also wishes to have large g-values in the excited state.

Zeeman laser-absorption spectroscopy was used to determine the relevant ground- and excited-state g-values that influence the Er^{3+}-Er^{3+} interactions responsible for optical dephasing.[19] Figure 7 schematically shows the Zeeman splitting for the ground (g) $^4I_{15/2}$:Z_1 and excited state (e) $^4I_{13/2}$:Y_1 levels, where g and e label the ground and excited state and + and − the upper and lower Zeeman components as shown in Fig. 7. The letters a, b, c, and d indicate the four different optical transitions that are possible between the levels. The g-values for the ground g_g and excited state g_e can then be extracted from the transition energies from Fig. 7 using

$$g_e = \frac{(E_a - E_b) + (E_c - E_d)}{2\mu_B B} \quad (1)$$

and

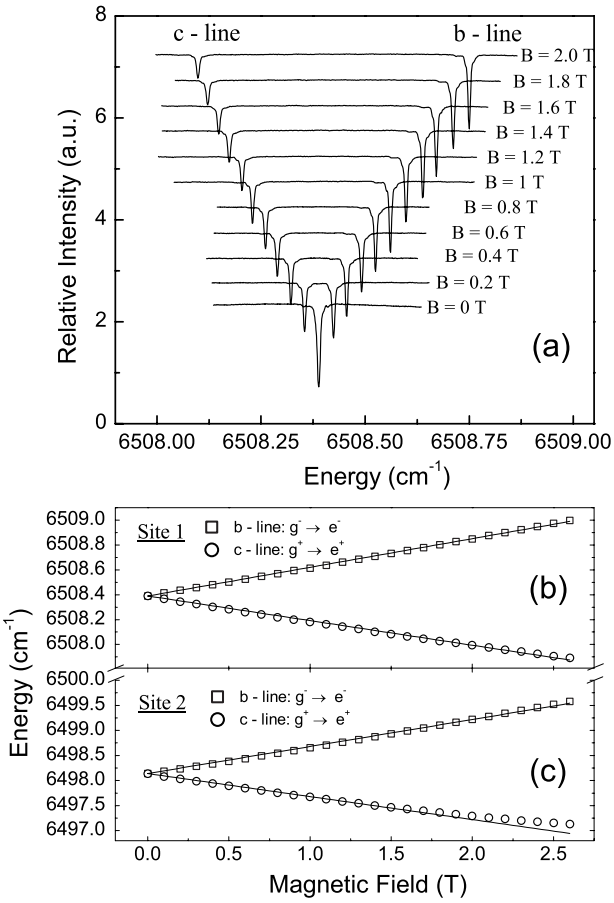

FIG. 8. Laser-absorption Zeeman spectra for 0.0015% $Er^{3+}:Y_2SiO_5$ as a function of magnetic field for $\mathbf{B}\|\mathbf{D}_1$ measured with $\mathbf{k}\|\mathbf{b}$ at $T=5$ K. (a) Sample laser-absorption scans for site 1 as the magnetic field is varied; subplots have been shifted vertically for better visibility. (b) Zeeman transitions for site 1 and (c) Zeeman transitions for site 2 as a function of magnetic field between $B=0$ and $B=2.6$ T; straight lines are fitted transition energies using Eqs. (3) and (4).

$$g_g = \frac{(E_a - E_c) + (E_b - E_d)}{2\mu_B B}, \tag{2}$$

where μ_B is the Bohr magneton and B is the magnetic field strength.

Figure 8(a) shows typical absorption spectra for transitions b and c for site 1, illustrating the outstanding resolution available. The subplots of sample spectra have been arranged vertically for better visibility. The spectral lines split as the magnetic field was increased linearly; the decrease of intensity for the c line was due to depopulation of the upper Zeeman level g+ with increased ground-state splitting. Transition energies in wave numbers are given in Fig. 8(b) for site 1 and Fig. 8(c) for site 2.

Application of a magnetic field splits each Kramers doublet differently, characterized by an anisotropic g tensor unique to each doublet. For high-symmetry sites, crystal symmetry dictates the orientation of the g tensor with respect to the crystallographic site axes. The Er^{3+} ion, however, has C_1 site symmetry at both crystallographic sites in $Er^{3+}:Y_2SiO_5$, and that does not place any restrictions on the g-tensors. Consequently, none of the principal g-tensor axes have to lie within a crystallographic plane or optical-polarization-extinction plane, and full angle-dependent Zeeman experiments, to be reported elsewhere,[32] were necessary to map out the g-values in the $\boldsymbol{D}_1$-$\boldsymbol{D}_2$, $\boldsymbol{b}$-$\boldsymbol{D}_1$, and $\boldsymbol{b}$-$\boldsymbol{D}_2$ planes and to determine the g-tensor components. For the particular situation where the magnetic field is aligned along the optical $\boldsymbol{D}_1$ axis in the crystal, we obtained a site 1 (site 2) ground-state g-factor of $g_g=5.5$ (15.0) and a site 1 (site 2) excited-state g-factor of $g_e=4.6$ (12.9). With this magnetic-field orientation, spectral diffusion has been successfully suppressed in SSH and/or SHB device applications.[5–10] Transition energies for the four different lines as a function of magnetic field are described by

$$E_{a,d} = E_0 \pm \frac{\mu_B}{2}(g_g + g_e)B \tag{3}$$

and

$$E_{b,c} = E_0 \pm \frac{\mu_B}{2}(g_g - g_e)B, \tag{4}$$

where E_0 is the zero-field transition energy between the $^4I_{15/2}:Z_1 \rightarrow {}^4I_{13/2}:Y_1$ crystal-field levels given in Table I and all other quantities have the same meaning as before. The straight lines in Figs. 8(b) and 8(c) are fitted using Eqs. (3) and (4). For higher magnetic fields, slight deviations from the linear behavior have been observed due to mixing with other nearby crystal-field levels.

V. CONCLUSIONS

Using site-selective spectroscopy, the crystal-field-level structure of the $^4I_{15/2}$ ground state and $^4I_{13/2}$ excited state were determined for both crystallographic sites in $Er^{3+}:Y_2SiO_5$. Long fluorescence lifetimes of the $^4I_{13/2}$ excited state were measured at 11.4 ms for site 1 and 9.2 ms for site 2. Zeeman experiments with the magnetic field along the $\boldsymbol{D}_1$ axis in the crystal gave a site 1 (site 2) ground-state g-factor of 5.5 (15.0) and a site 1 (site 2) excited-state g-factor of 4.6 (12.9). Using laser absorption experiments, very sharp inhomogeneous linewidths of 180 MHz in 0.0015% $Er^{3+}:Y_2SiO_5$, 390 MHz in 0.005% $Er^{3+}:Y_2SiO_5$, and 510 MHz in 0.02% $Er^{3+}:Y_2SiO_5$ were measured.

The properties reported here, together with the measurements of optical coherence and spectral diffusion that we reported earlier, make $Er^{3+}:Y_2SiO_5$ a particularly interesting material for SSH signal-processing. The narrow homogeneous linewidths and modest spectral diffusion provide precise frequency resolution, while tailorable inhomogeneous linewidths provide large signal-processing bandwidth. The narrow inhomogeneous linewidths provide interesting frequency references even at elevated temperatures, and when combined with the narrow homogeneous linewidths and modest spectral diffusion, they provide an interesting hybrid laser frequency stabilization scheme for SSH devices and for other applications like vibrometry and light detection and ranging (LIDAR).

ACKNOWLEDGMENTS

The authors are grateful to R. W. Equall and R. L. Hutcheson of Scientific Materials Corporation of Bozeman, Montana for providing the crystals. All experimental measurements were conducted at Montana State University. This research was supported by AFOSR Grant No. F49620-01-1-0313 and the Montana Board of Research and Commercialization Technology. T. B. wishes to acknowledge financial support from the University of San Francisco faculty development fund.

*Permanent address: Department of Physics, University of San Francisco, 2130 Fulton Street, San Francisco, CA 94117, USA. Electronic address: tbottger@usfca.edu

†Present address: Department of Physics, University of South Dakota, Vermillion, SD 57069, USA. Electronic address: ycsun@usd.edu

‡Electronic address: thiel@physics.montana.edu

§Electronic address: cone@montana.edu

[1] Thomas Böttger, Y. Sun, C. W. Thiel, and R. L. Cone, Proc. SPIE **4988**, 51 (2003).

[2] Y. C. Sun, in *Spectroscopic Properties of Rare Earths in Optical Materials*, edited by Guokui Liu and B. Jacquier (Springer-Verlag, Berlin, 2005), p. 379.

[3] C. Li, C. Wyon, and Richard Moncorge, IEEE J. Quantum Electron. **28**, 1209 (1992).

[4] R. M. Macfarlane, T. L. Harris, Y. Sun, R. L. Cone, and R. W. Equall, Opt. Lett. **22**, 871 (1997).

[5] T. L. Harris, Y. Sun, R. L. Cone, R. M. Macfarlane, and R. W. Equall, Opt. Lett. **23**, 636 (1998).

[6] T. L. Harris, Y. Sun, W. R. Babbitt, R. L. Cone, J. A. Ritcey, and R. W. Equall, Opt. Lett. **25**, 85 (2000).

[7] P. B. Sellin, N. M. Strickland, T. Böttger, J. L. Carlsten, and R. L. Cone, Phys. Rev. B **63**, 155111 (2001).

[8] Thomas Böttger, Y. Sun, G. J. Pryde, G. Reinemer, and R. L. Cone, J. Lumin. **94–95**, 565 (2001).

[9] G. J. Pryde, T. Böttger, and R. L. Cone, J. Lumin. **98**, 309 (2002).

[10] Z. Cole, T. Böttger, R. Krishna Mohan, R. Reibel, W. R. Babbitt, R. L. Cone, and K. D. Merkel, Appl. Phys. Lett. **81**, 3525 (2002).

[11] V. Crozatier, V. Lavielle, F. Bretenaker, J.-L. Le Gouët, and I. Lorgeré, IEEE J. Quantum Electron. **40**, 1450 (2004).

[12] V. Crozatier, G. Gorju, F. Bretenaker, J.-L. Gouët, and I. Lorgeré, Opt. Lett. **30**, 1288 (2005).

[13] B. R. Judd, *Operator Techniques in Atomic Spectroscopy* (McGraw-Hill, New York, 1963).

[14] B. G. Wyborne, *Spectroscopic Properties of the Rare Earth* (Interscience, New York, 1965).

[15] G. H. Dieke, *Spectra and Energy Levels of Rare-Earth Ions in Crystals* (Wiley, New York, 1968).

[16] S. Hüfner, *Optical Spectra of Transparent Rare Earth Compounds* (Academic Press, London, 1978).

[17] H. A. Kramers, Proc. Acad. Sci. Amsterdam **33**, 959 (1930).

[18] Thomas Böttger, Ph. D. thesis, Montana State University, 2002.

[19] Thomas Böttger, C. W. Thiel, Y. Sun, and R. L. Cone, Phys. Rev. B **73**, 075101 (2006).

[20] B. A. Maksimov, Yu. A. Kharitonov, V. V. Ilyukhin, and N. B. Belov, Sov. Phys. Dokl. **13**, 1188 (1969).

[21] Y. Sun, F. Könz, R. L. Cone, and R. W. Equall (unpublished).

[22] Obtained from the HITRAN database of the Harvard-Smithsonian Center for Astrophysics.

[23] Data analysis software by C. W. Thiel.

[24] H. Sasada and K. Yamada, Appl. Opt. **29**, 3535 (1990).

[25] M. D. Levenson and S. S. Kano, *Introduction to Nonlinear Laser Spectroscopy* (Academic Press, New York, 1988), p. 228, and references cited therein.

[26] R. M. Macfarlane, A. Z. Genack, and R. G. Brewer, Phys. Rev. B **17**, 2821 (1978).

[27] R. D. Shannon, Acta Crystallogr., Sect. A: Cryst. Phys., Diffr., Theor. Gen. Crystallogr. **32**, 751 (1976).

[28] Y. Sun (unpublished).

[29] F. Könz, Y. Sun, C. W. Thiel, R. L. Cone, R. W. Equall, R. L. Hutcheson, and R. M. Macfarlane, Phys. Rev. B **68**, 085109 (2003).

[30] Thomas Böttger, G. J. Pryde, C. W. Thiel, and R. L. Cone (unpublished).

[31] Thomas Böttger, C. W. Thiel, Y. Sun, and R. L. Cone (unpublished).

[32] Y. Sun, Thomas Böttger, C. W. Thiel, and R. L. Cone (unpublished).